Additive Manufacturing 95 (2024) 104549

Contents lists available at ScienceDirect

Additive Manufacturing

journal homepage: www.elsevier.com/locate/addma

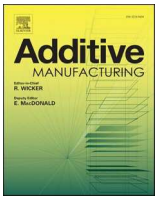

Realizing arbitrary 3D microarchitectures with curved and near-sharp segments via toolpath strategies in aerosol jet printing

Sandra M. Ritchie [a], Chunshan Hu [a], Rahul Panat [b,*]

[a] Department of Mechanical Engineering, Carnegie Mellon University, Pittsburgh, USA
[b] Robotics Institute, Carnegie Mellon University, Pittsburgh, USA

ARTICLE INFO

Keywords:
Aerosol Jet printing
Additive manufacturing
3D microarchitectures
Metal
Microprinting
3D structures

ABSTRACT

Aerosol Jet (AJ) printing is a jetting-based additive manufacturing (AM) technique that uses droplets in an aerosol form to deposit nanoparticles or polymer inks at a length scale of about 10 micrometers. The desired structural geometries via AJ printing can be obtained at a high efficiency and accuracy by engineered toolpaths and fill strategies. Recently, AJ printing is used to create three-dimensional (3D) freestanding microarchitectures such as microlattices, spirals, walls, and micropillars without any auxiliary support during printing. In this work, we demonstrate that for curved segments, the difference in the printed material volume on the convex side vs concave side leads to the accumulation of material while building freestanding 3D microarchitectures. This effect is most severe for sharp corners, which leads to build-defects such as protrusions and voids. We carry out a systematic study of the material accumulation on curved segments of AJ printed 3D microarchitectures. For 3D microwall segments with sharp curved portions, a positive (or negative) material accumulation causing large overgrowths (or voids) as a function of the angle between the tangents on the two sides of the microwalls and the radii of curvature are studied. For sharp bends ($<15^\circ$) in the microwalls, adding a radius of curvature may not be sufficient to avoid overgrowths and voids, and the lines can be considered as individual segments. For microwall bends with $>45^\circ$ angle between the segments, smaller radii of curvature can be tolerated. We conclude that a fillet radius equal to the line width for 30° angles is necessary to avoid accumulation and therefore the protrusion defects. A simple model based on mass-conservation is also developed which shows the importance of considering ink self-leveling during printing. This information is then used for toolpath strategies to avoid defects on sharp curved microwall segments for complex 3D architectures such as protruding star shape and Scotty Dog, the Carnegie Mellon University mascot. This research will enable the defect-free fabrication of highly complex 3D microarchitectures via jetting-based AM techniques such as AJ printing.

1. Introduction

Additive manufacturing (AM), colloquially known as 3D printing, encompasses a wide range of technologies where material is deposited in a layer-by-layer fashion to create 3D shapes. This is in contrast with subtractive manufacturing techniques that remove material from a starting billet to create the desired shape. AM allows the creation of complex architectures, material combinations, and controlled material properties, with significant ongoing development for polymer [1,2], metal [3–5], and ceramic [6,7] materials at multiple length scales. AM processes can be divided into many categories based on the overall process design, but for the purposes of this study, we will separate them based on one key difference – whether a layer of material (powder, resin, etc.) fills the entire build chamber and directly defines the layer thickness, such as in powder bed fusion or vat polymerization, or whether material is deposited in the build chamber only where the part (and supports, if applicable) is located, such as in material extrusion or jetting techniques.

In AM, parts are typically modeled in CAD software and then 'sliced' into layers that are built successively to form the part. Within each of the layers, a fill strategy (or some combination of strategies) must be used in order to achieve solid features, such as hatching, checkerboard, or contour. This toolpath strategy then defines a raster/path for either the laser (i.e., the source of energy) for laser-powder-bed-fusion AM or the nozzle (i.e., source of material to be deposited) in case of extrusion or jetting-based AM. The toolpath directly affects processing time as idle

* Corresponding author.
E-mail address: rpanat@andrew.cmu.edu (R. Panat).

https://doi.org/10.1016/j.addma.2024.104549
Received 13 December 2023; Received in revised form 11 October 2024; Accepted 11 November 2024
Available online 13 November 2024
2214-8604/© 2024 The Author(s). Published by Elsevier B.V. This is an open access article under the CC BY-NC-ND license (http://creativecommons.org/licenses/by-nc-nd/4.0/).

time can be a significant portion of the total print time. Moreover, the toolpath affects part quality/yield, geometric accuracy, and material properties – and thus print capability and part cost [8]. In material extrusion or material jetting processes, the toolpath strategies affect local layer height which is not predetermined by the spreading/filling of source material. These effects are complex and can depend on both method and material. For laser-powder-bed-fusion, scan strategy affects the heat build-up within the part and therefore warping behavior, feature sizes, dross, and melt-pool phenomena such as keyholing [9,10].

In material extrusion, material jetting, or directed energy deposition, overfilled and/or underfilled regions can be formed, particularly at corners or bends, i.e., the locations where toolpath changes trajectory. This is because the material flow is not infinitely narrow and thus cannot necessarily be accurately treated as a *zero-dimensional* point or *one-dimensional* line, i.e., *the path length on the inside (concave side) of a corner can be significantly shorter than the path length on the outside (convex side) of the same corner* depending upon the sharpness of the bend and the angle between the proximate and regressing line segments. Building of 3D microwalls via successively stacking material on such lines can then accumulate this effect. This effect can become more acute in cases where (1) the dimensions of the material flow are similar to the finished part dimensions, such that single line or 'small' defects are on the same length scale as the desired features and/or (2) printed material dries or solidifies quickly, preventing self-leveling from canceling this effect. Our work will focus on this very process regime.

Different strategies have been developed in literature to address the issue of material accumulation, particularly for extrusion-based processes such as fused deposition modeling of thermoplastics [11,12]. One such strategy involves limiting the use of sharp corners by adding radii, which is effective, but adds significant limitations to part design especially for small parts where the radii can be at a similar length scale as the finished product. This also brings to question how to determine what radius is required based on a given design. For solid parts, different in-contour fill strategies and non-equidistant spacing between printed lines, sometimes incorporating varying line widths, can be used to avoid large underfilled regions and allow a small amount of material flow during printing to partially fill-in gaps [13–16]. This method is effective at reducing large-scale defects within a printed layer but does not address the defects in the layer thickness, which can also affect part quality, particularly in cases of high layer numbers. Use of small layer thickness and a reduction in the viscosity of the printed material by increasing nozzle temperature are other methods to reduce voids but can increase print time and decrease geometric accuracy [17,18]. Another method (often used in tandem) is the rotation or offset of hatch fill with each layer. This prevents positive interference of small defects from turning into larger defects as would happen if each layer was printed identically. Once again, this is effective in many cases but is not feasible for long narrow structures.

Recently, aerosol jet (AJ) printing has emerged as a 3D AM technique with the capability of producing features and parts across a variety of length scales. Minimum line width achieved by this technique is 10 μm, and printed parts can reach up to a centimeter or more in overall size, with layer thicknesses varying from 100 nm to microns [19]. In the past, AJP was used to fabricate films or interconnects on planar or curved 3D surfaces, with good repeatability[20–30]. This capability was extended to AJ printed freestanding 3D structures fabricated without auxiliary support by our group to achieve complex microarchitectures such as microlattices, micropillars, and spirals [31–34]. These structures have been used to introduce a new mechanism for 4D printing via unconstrained sintering [34]. Further, several exciting applications have been enabled by freestanding AJ printed 3D structures in the application areas of brain-computer interfaces [33], world's fastest and highly sensitive biomolecule detection [35,36], high-capacity Li-ion batteries [37], structural materials [38], and 3D electronics packaging [39,40]. We note that precise 3D structures are needed for these applications. For example, in case of AJ printed brain-computer interfaces, precise shaping of the shank tips of the device controls their seamless entry into the brain tissue and depends upon precision in material deposition during the planning toolpath [33]. Similarly, precise AJ material deposition is known to control fillets and interconnects in 3D electronics packaging applications [40].

The repeatability and stability of aerosol jet printing have proven to yield uniform layer thicknesses in 2D printed lines [41–44]. These studies, however, have not yet considered the geometric effects of toolpath strategies when moving into the third dimension. In our prior work on AJP 3D structures [32–34], pillar arrays and scaffolds were produced by serially printed semi-circles which are rotated with each layer. This method is effective and produces high-quality parts within these selected geometries [31], but there does not yet exist a robust method for determining appropriate toolpaths for arbitrary geometries such as walls with sharp bends that would avoid significant geometric defects such as large-scale voids and protrusions. These defects are often geometrically coupled as protrusions can 'grab' droplets before they reach the intended deposition location, thus forming larger voids. Although additional post-steps could potentially remove protrusions, this would not address the issue of voids. This has led to design constraints in jetting and extrusion-based AM techniques that need to be addressed.

In this paper, we present a systematic experimental study of the effect of toolpath strategy on part quality for the AJ printing technique. We consider the defects introduced when printing curved 3D microwall segments where the difference in the printed material volume on the convex side vs. concave side leads to the accumulation of defects. The effects of angle between the tangents on the two sides of the segment and the radius of curvature are studied. The results are applicable to a large set of conditions with minimal experimentation and without computationally intensive physics-based modeling. The results will be of specific interest in the development and characterization of new inks as the print quality can be predicted a priori, saving on the trial-and-error experimentation and the nanoparticle ink consumed. We then demonstrate defect-free printing of complex 3D shapes such as a star and Scotty Dog, the CMU mascot, upon application of these strategies.

2. Materials and methods

2.1. Aerosol jet printing and toolpath strategy

All structures in this work were printed using a commercially available silver nanoparticle ink (JS-A221AE, Lot 102819–001, Novacentrix, Austin, TX). Silver was chosen because of the importance of freestanding 3D silver structures in technologies such as brain-computer interfaces [45], high-sensitivity biomolecule detection [46], interconnection/vias in microelectronics [47], and studies of shape distortion in AM [34]. The as-purchased ink had a viscosity of 8.3 cP, an average particle size of 47 nm, and 50 % silver content by weight per the supplier data sheet. To demonstrate the generality of our approach, we also printed silver ink from another supplier (PRELECT TPS 30, Clariant, Germany) and ZnO ink (Sigma-Aldrich, St. Louis, MO). The ZnO ink had an average particle size of 40 nm with largest particle < 100 nm, and a particle loading of 20 wt% in H_2O. The inks were diluted with de-ionized water at a ratio of 3:1 for all cases to improve printability. All features and structures were fabricated using an Aerosol Jet 3D printer (Model AJ-300, Optomec, Inc., Albuquerque, NM) as shown in Fig. 1a. For the AJ printer, the platen moves in the *x-y* plane according to the printing program while the nozzle can be moved manually in the *z*-direction. The nozzle diameter was 150 μm, and the ultrasonic atomizer (frequency: 1.7 MHz, with current output of 600 mA) was used in the AJ printer. All samples were printed with a platen temperature of 70°C. This temperature was chosen as sufficient for the building of 3D features via AJP while maintaining compatibility with many materials. Carrier gas flow was 40–55 SCCM, and sheath flow was 18–22 SCCM. The droplet flow through the nozzle of the AJ printer is continuous and printing patterns

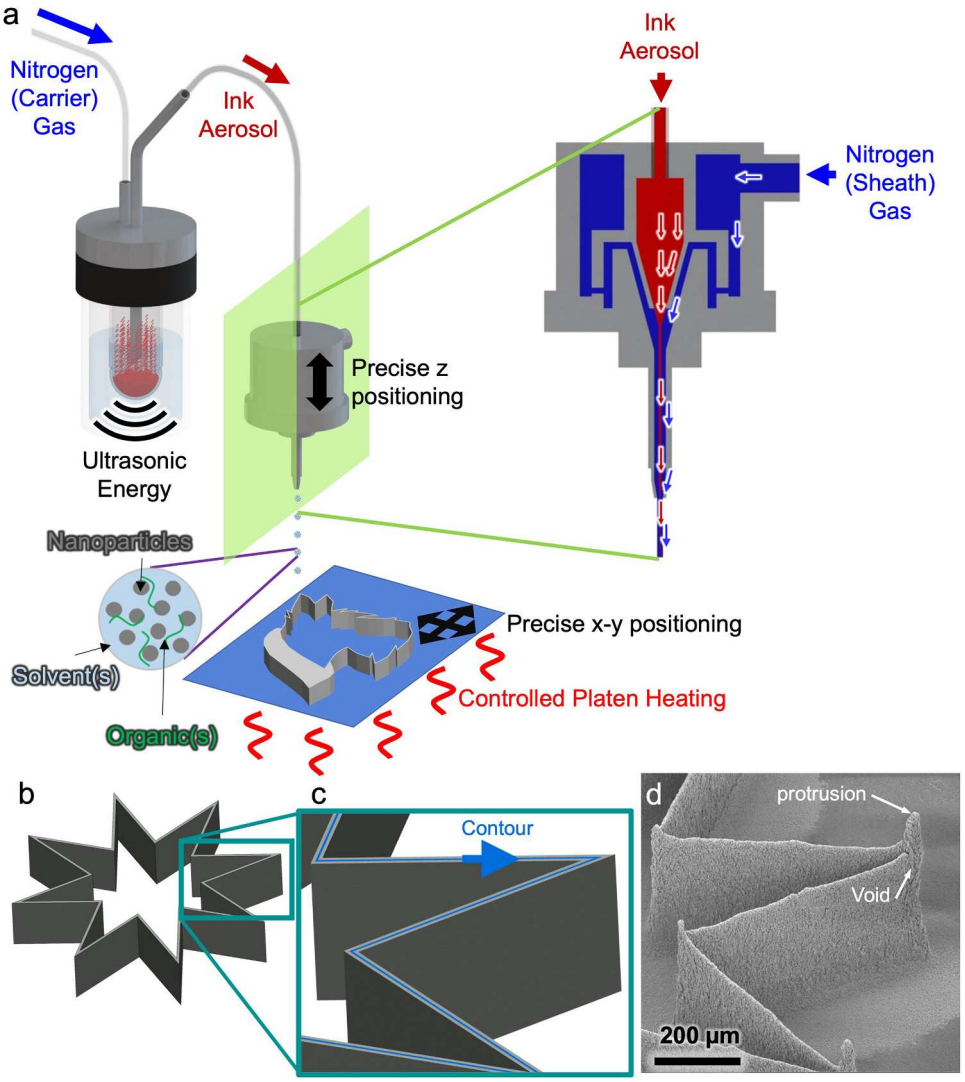

Fig. 1. Aerosol Jet (AJ) printing process and defect examples. (a) Schematic of the AJ printing process used in this work. The ultrasonic atomizer is used to aerosolize silver nanoparticle ink. The aerosol is carried to the deposition head where the material stream is focused by the sheath gas flow. Microdroplets are then deposited on a moving platen which is heated to rapidly dry the printed material (b) A CAD schematic of an 8-pointed star. (c) Inset showing toolpath contour which is the 2D cross-section of the design in (b). (d) AJ printed 3D star geometry using the toolpath shown in (c). In the regions where sharp corners are used in the toolpath, there is a large protrusion and adjacent void.

are achieved via a shutter that can break the aerosol flow as per the printing program. The time scale of the shutter motion is about 2 ms according to the equipment data sheet. All samples were printed on alumina substrates, with the single pass samples on finely ground alumina (CmAl2O3767605S1, MTI Corporation, Richmond, CA) with a surface roughness, R_a, of <100 Å per the supplier data. Print speed was maintained at 1 mm/s for these samples.

Printed geometries were first conceptualized based on a final 3D shape (Fig. 1b), and this was translated into 2D polylines in AutoCAD. Outlines were then filled in (Fig. 1c) for solid areas, using either offset lines or serpentine patterns. These files were then converted to a "prg" file which can be read by the printer software. An example printed star shape comprised of microwalls with sharp angles in the *x-y* plane based on the outlines in Fig. 1c with apparent defects is shown in Fig. 1d.

Single lines with one pass were printed using AJ printing. On one substrate, five different angles (15°, 30°, 45°, 90°, and 135°) are studied with fillet radii ranging from 0 μm up to 1 mm, each. Note the largest radii of 500 μm and 1 mm were not considered for the smaller angles as they would no longer bare any resemblance to the desired geometry. Each condition has five repetitions. Additional vertical and horizontal lines are added to allow for easy alignment in the optical surface profiler. A line width of 35 μm was used for compatibility with the optical surface profiler (pixel size of approximately 4 μm). A short printing time (<20 minutes) was maintained in order to avoid any effects of process drift.

2.2. Optical profilometry and imaging

In order to capture the effects of overfill and underfill in the corners, single line passes were created and characterized while independently varying angle and fillet radius (see Figs. 2a and 2b for schematic and sample design). Single pass samples were characterized via optical profilometry (VR 5200, Keyence, Itasca, IL) at a magnification of 160×. See Fig. 2c-g for examples of the profilometer data that provides the height. The region of interest (ROI) lengths for measurement varied from 150 μm to 1000 μm. Considering the location variability for the measurement was +/-2 μm, this translated to a variation in measurement of <2 % for all the cases. Note that the alumina substrate was compatible with the optical profilometry as it was neither transparent nor highly reflective. From the profilometer software, the point cloud

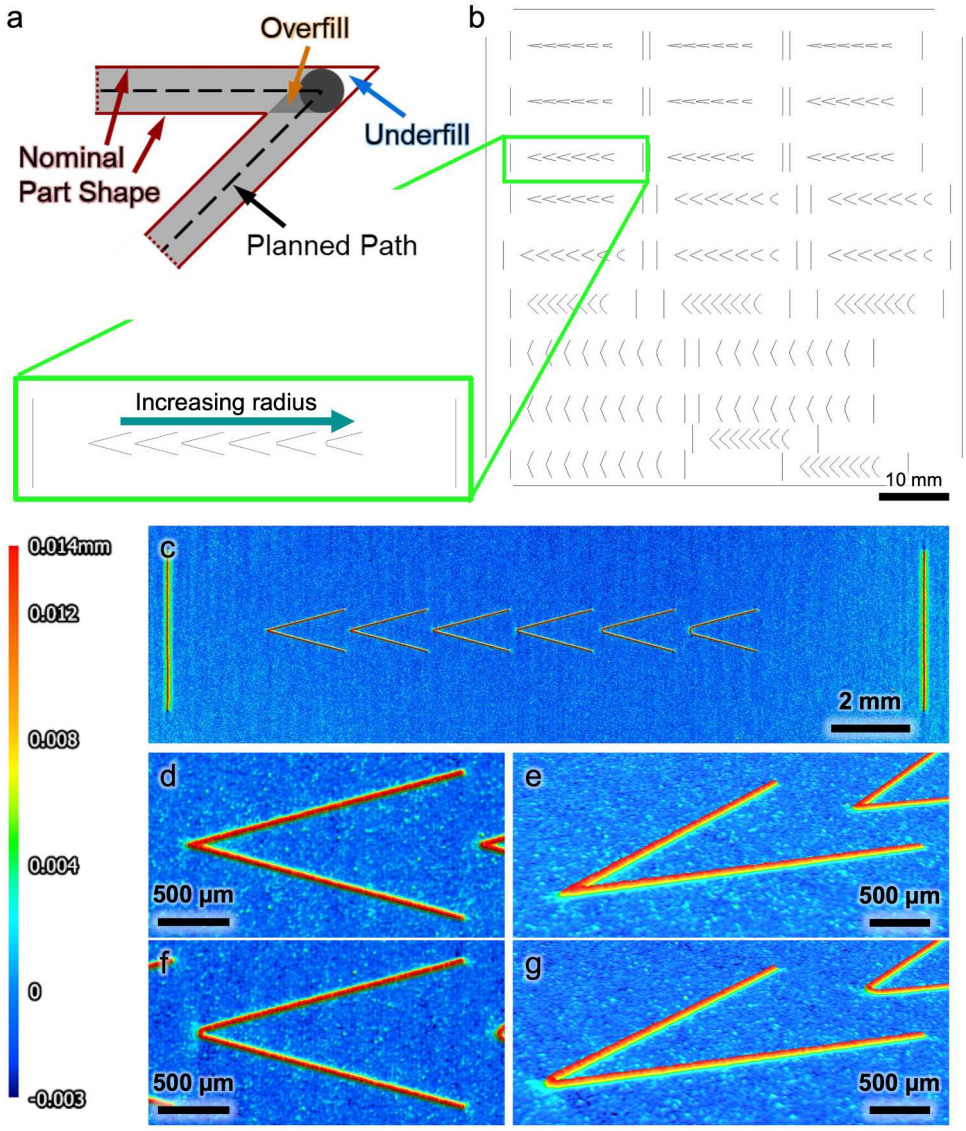

Fig. 2. Geometry of AJ printed 2D lines. (a) Schematic of a sharp corner for a planned toolpath showing overlapped inside corners and underfilled outside corners. The overlapping region is expected to have an overfill, while the void region is expected to have an underfill relative to the straight-line cross-section. (b) CAD drawing of the experimental design for the AJ printed 2D lines. On one substrate, five different angles (15°, 30°, 45°, 90°, and 135°) are studied with fillet radii within the toolpath ranging from 0 µm up to 1 mm. Each condition has five repetitions. Additional vertical and horizontal lines are added to allow for easy alignment in the optical surface profiler. (c) Representative quantitative surface profile data for the printed lines at 30° with a single pass. (d, e) Close-up images from (c) for the case of 0 applied radius. (f, g) Close-up images from (c) for the case of 30 µm applied radius.

data was exported and subsequently imported into Matlab software (MathWorks, Natick, MA) for full analysis. Each printed angle was individually aligned, and any baseline tilt in the substrate was removed. The Matlab code from these operations is provided in Supporting Information. SEM images were obtained using a FEI Quanta 600 FEG (FEI Company, Hillsboro, OR).

2.3. Data analysis

In order to study the geometric effects in tight corners, it might seem instructive to look at individual cross-sections at the corners. However, overfill and underfill make it difficult to compare cross-sections between different conditions as the geometric center of such cross-sections does not necessarily correlate with the programmed toolpath. In addition, such measurements would be overly affected by any small surface roughness measured in the samples (whether real or an effect of instrument precision). As such, it is more useful to consider volumes and their average heights as discussed below. Volumes were determined by a region of interest, ROI, which, in turn, is defined by the length between points A and B in Fig. 3a, where A and B are equidistant from the midpoint of the feature and on the centerline, or planned toolpath. By studying a range of ROIs, the effects very close to the corner as well as overall effects can be studied. Within these volumes, we can further divide the analysis based on areas inside the toolpath and outside the toolpath (purple and blue regions of Fig. 3a, respectively). The average height within these volumes can also be measured to identify the accumulation effects.

All combinations of angle and radii have five replicates within the data set, and volume and height measurements for each replicate are averages of the pixels identified in multiple segments in the ROI. Since the number of pixels varies with the length of the ROI from tens to thousands for each replicate, an exceedingly rich set of data is obtained through these measurements.

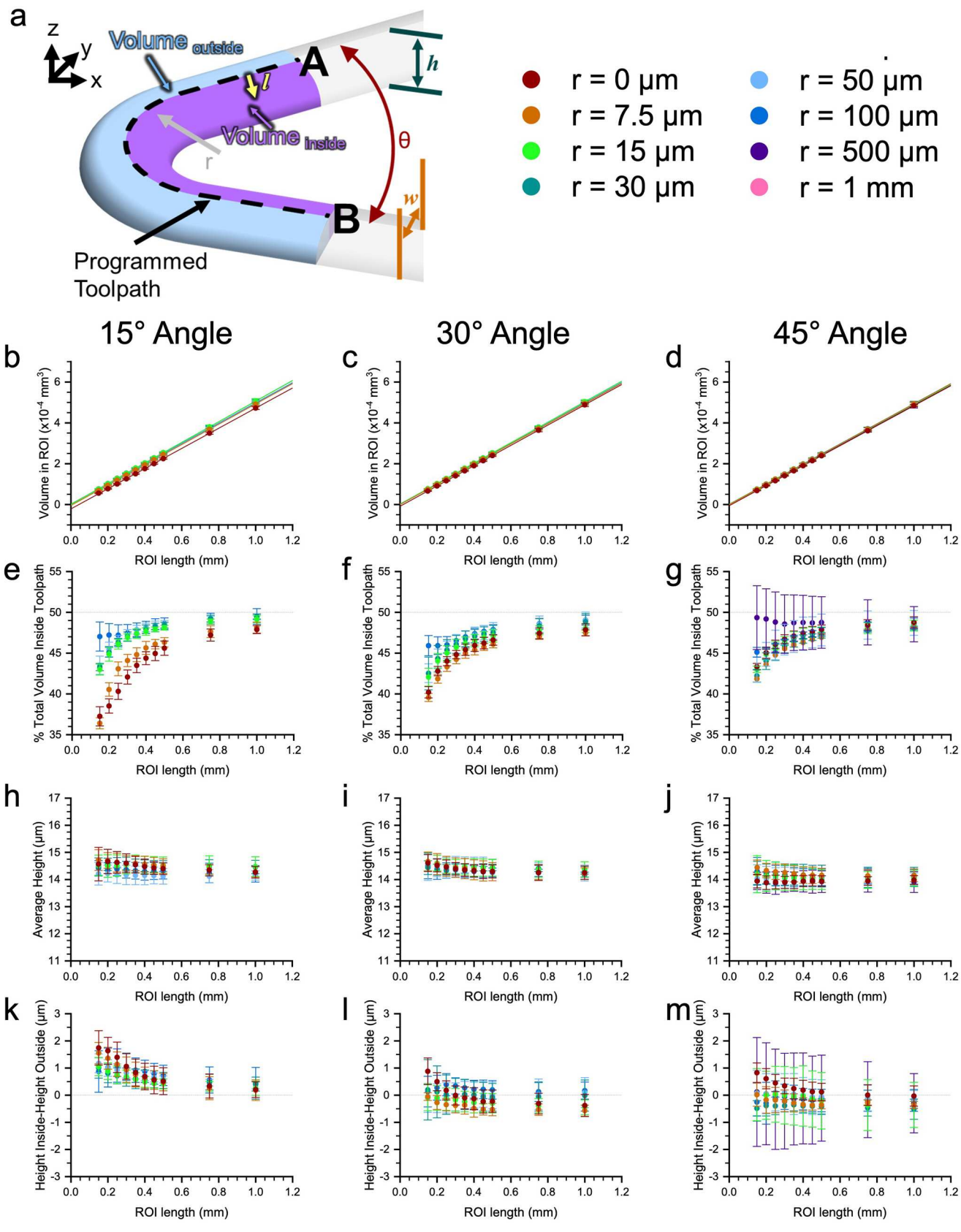

(caption on next page)

Fig. 3. Volume and height data from single pass printed lines. **(a)** Schematic showing the Region of Interest (ROI) which is defined as the path length from A to B, where A and B are equidistant from the projected intersection point. These regions are then considered separately and together to compare volumes and average heights. Also shown are variables used in the mathematical model. **(b-d)** Total volume of AJ printed lines within the ROI for bend angles of 15°, 30°, and 45°, respectively. Linear fits of the data are also shown. Linear changes in volume with ROI length proves consistent deposition rates and that stage acceleration and deceleration at the bent sections are not important factors in this study. **(e-g)** Percent of total volume of the AJ printed lines found on the inside of the toolpath for 15°, 30°, and 45°, respectively. Deviations from 50 % mark indicates the effect of material self-leveling during drying. **(h-j)** Average height of printed lines (including volumes on inside and outside) within the ROI for lines with bends at 15°, 30°, and 45°, respectively. **(k-m)** Height difference between inside and outside volume of the toolpath for lines with bends at 15°, 30°, and 45°, respectively. All data points in this figure represent the average and standard deviation across five replicates. The data from each replicate is an average of pixels within the ROI, with the number of pixels changing with the ROI length from tens to thousands. Similar results for AJ printed lines that bend at 90°and 135° are given in Supplementary Fig. S2.

3. Results and discussion

The fluid dynamics of AJ printing process has been described by Secor [48]. In AJ printing, the stream of gas containing the droplets with metal nanoparticles (i.e., the aerosol) exits the nozzle at a speed of the order of 100 m/s; with <1 % of the total gas stream consisting of the droplets. Each droplet has a diameter of 1–5 μm. Each of the droplets contains about 60–70 % active material [31], with the rest of being solvents and proprietary binders. It is expected that the solvents undergo evaporation during the flight from the vial to the nozzle [31]. The Reynolds number for the droplets is low, <600 [49], leading to viscous droplets creating the 3D structures. Through such a complex phenomenon, the 3D freestanding patterns are built in a layer-by-layer manner (i.e., AM at microscales). Although the detailed models underlying the AJ deposition process are beyond the scope of this paper, we expect material to accumulate in the overlapping sections of the toolpath at a bend as shown in Fig. 2a; while the dynamics of drying will determine the leveling effect. We now describe the results of our experiments and discuss their implications.

3.1. Effect of stage motion on print volume

One of the first focus areas of this study was determining whether stage acceleration and deceleration at corners of a segment results in a significant amount of extra material being deposited in the corners (or not). This has been a cause of print defects in extrusion printing and laser cladding processes [50,51]. For all angles and radii studied in this work (Fig. 3), the volume was measured for a variety of ROI lengths. It was found in all cases that the volume changed linearly with ROI length, and the best fit lines in all cases did not have a large positive intercept (see Fig. 3b-d and Supplementary Fig. S1a-c, and S2a, b). This represents data from 175 AJ printed lines. As such, this effect can be neglected in the case studied here.

Note that the response time for the shutter open/close which controls the printing of lines/patterns in AJ is 2 ms. For a deposition rate of 10–100 of nL/min [48,52], the deposition within the shutter response time could range from negligible (hundreds of nanometers in height) to significant (several micrometers in height) depending upon the printing speed. This is important conclusion for both closed and open printed contours, especially for ROI $\geq$ 100 μm, used in this study.

3.2. Leveling effects

Depending on the platen temperature and volatility of the ink solvent, the deposited microdroplets form a fluid layer that dries at a certain time scale. This is one of the reasons that adding a cosolvent (such as diethylene glycol) to the ink can improve print quality by allowing each layer to self-level before fully drying during the AJ printing. When considering 3D features, however, slow drying can limit the printing speed, overhang angle, and resolution, requiring further heating of the platen. The amount of self-leveling determines the extent to which ink volume is redistributed between the two sides of the center line. Printed straight lines are symmetric about the center of the material stream, meaning that without leveling effects, equally deposited volumes are expected on either side of the center line. For bent lines, however, we see significant differences in the deposited volume with more than 10 % of the volume moving from the inside to the outside in some cases (Fig. 3e-g and Supplementary Fig. S2c-d), even with a platen temperature of 70°C when evaporation is expected to be rapid for the AJ droplet sizes [34].

3.3. Height measurements and differences

The average line height for the printed structures in Fig. 2b was about 14 μm (see Fig. 3h-j and Supplementary Fig. S2e-f) with a line width of about 35 μm. This is consistent across all angles and radii, with no overall trend as a function of the ROI length. Height differences measured between the volume inside and outside are on the order of a couple microns in the most severe cases (see Fig. 3k-m and Supplementary Fig. S2g-h), or up to 12 % of the overall height. This difference becomes negligible for large ROI lengths as the straight regions within the ROI dominate the average value. For the smallest angle, θ, in this study (15°), even the largest studied radius at the corner of 100 μm shows a measurable height difference at small ROI lengths. This result shows that for such small angles between the lines, adding a radius may not be sufficient to avoid overgrowths and voids, and the lines can be considered as individual segments. For $\theta = 30°$, a radius of 7.5 μm shows a marked improvement over no planned radius while a radius of 30 μm or larger (comparable in size to the line width) shows no measurable height difference, even at the smallest ROI length. For 45° angles, the required radius is even smaller at 15 μm (less than half of the line width) to show no measurable height difference between the convex and concave sides. In the other use cases studied here, 90° and 135°, no measurable height difference is observed, even without adding a corner radius in the toolpath (see Supplementary Fig. S2g, h).

3.4. Geometric model

As seen in Fig. 2a, the cause of the overfill and underfill at sharp segments is the difference in effective path length, and therefore effective velocity, through the line width, with the inner side having a shorter length and therefore slower speed and vice versa. As such, modeling the effect geometrically starts by calculating the difference in path length through the line thickness. For this model, we are assuming a line width which is uniform throughout the cross-section for straight sections without angles, a reasonable approximation based on experimental observations. Inputs include line width (w), line height (h), angle (θ), radius (r), and length of the ROI (l_{ROI}) as defined in Fig. 3a and Fig. 4a. Additionally, the model requires a number of sections, n, to divide the line width into. Here, we take $n = 100$ as this was shown to be sufficient for convergence. The output we are using to compare with experimental data is the average height inside and outside of the toolpath line.

The first step in the model is determining the vector of perpendicular distances, l, from the center toolpath line to the outer edge of the printed line (see Fig. 4a). This vector, l, is determined as an equally spaced vector from $-w/2$ (on the outside of an angle) to $w/2$ (on the inside of an angle), with n number of segments. Note that by defining n as an even number, the value 0 will not appear in this vector, meaning that the ROI is neatly divided with no locations overlapping the toolpath itself.

We then define the radius, R, for the individual location of l.

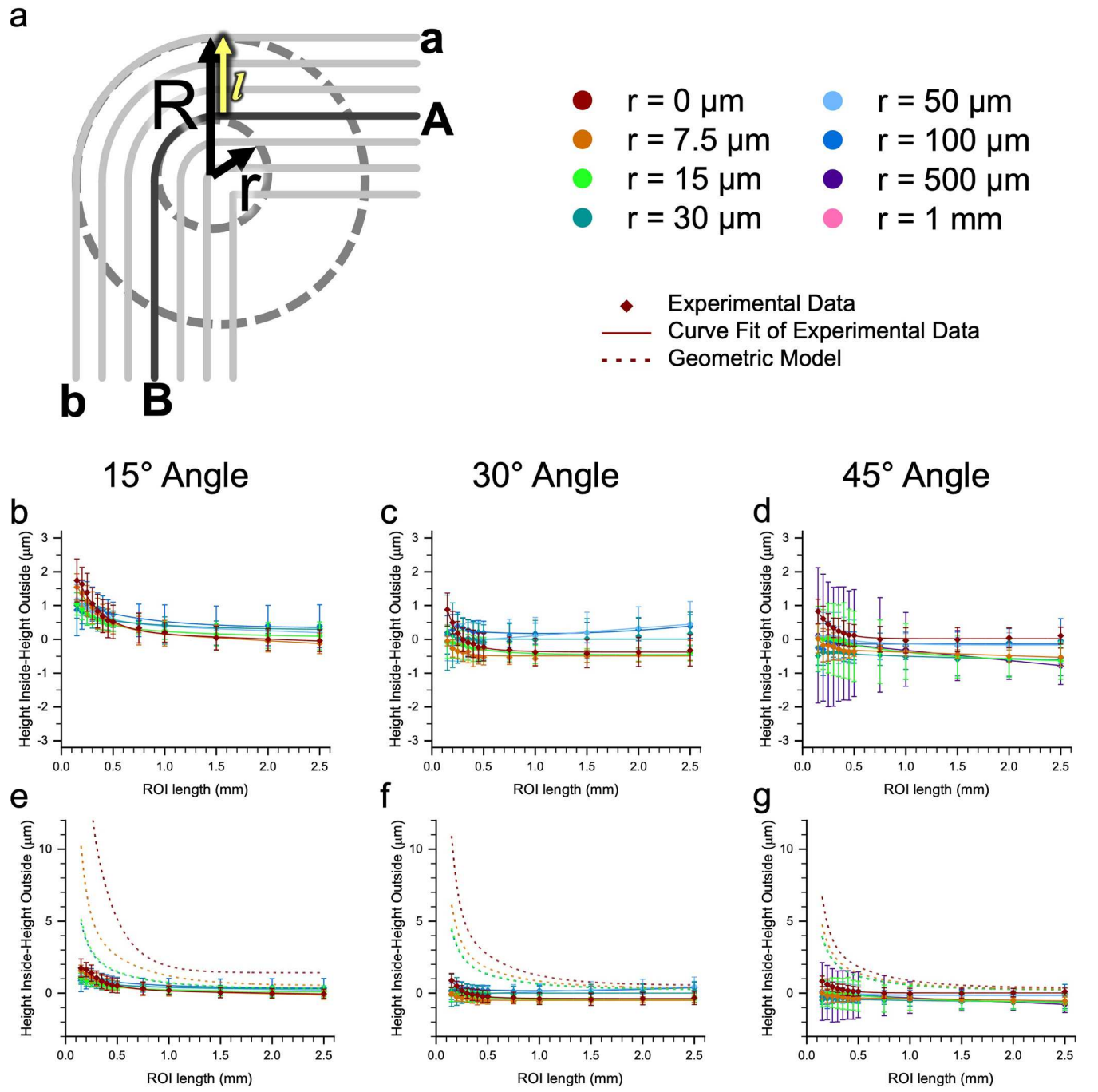

Fig. 4. Exponential decay fit and comparison with geometric predictions. **(a)** Schematic defining variables used in the mathematical model. **(b-d)** Experimental data from Fig. 3k-m with exponential decay fit for 15°, 30°, and 45°, respectively. **(e-g)** Predicted height differences from geometric model with assumption of no self-leveling during drying for 15°, 30°, and 45°, respectively. Clearly, the model overpredicts the height difference seen in experiments by an order of magnitude, highlighting the importance of the self-leveling effect. All experimental data points in this figure represent average and standard deviation across five replicates. The data from each replicate is an average of pixels within the ROI, with the number of pixels ranging from tens to thousands depending upon the ROI length. Similar results for AJ printed lines that bend at 90°and 135° are given in Supplementary Fig. 2.

$$R = \begin{cases} 0 & \text{if } l \geq r \text{ and } l \geq 0 \\ r - l & \text{else} \end{cases} \quad (1)$$

We then consider the vector Δ as the effective path length for a given value of l (e.g., Δ is the length of the line between a and b in Fig. 4a). Note these equations are written where θ is in radians.

$$\Delta = \begin{cases} l_{ROI} - r \times (\pi - \theta) - 2 \times \dfrac{l - r}{\tan(\frac{\theta}{2})} & \text{if } R = 0 \\ l_{ROI} + (R - r) \times (\pi - \theta) \end{cases} \quad (2)$$

We then sum the values of Δ separately for all l on the inside (concave side) and outside (convex side) of the toolpath to calculate the total length inside and outside of the toolpath as L_{in} and L_{out}, respectively. We then define the relative deposition rate for inside and outside of the

toolpath as d_{in} and d_{out}.

$$d_{in} = \frac{L_{out} + L_{in}}{2 \times L_{in}} \tag{3}$$

$$d_{out} = \frac{L_{out} + L_{in}}{2 \times L_{out}} \tag{4}$$

This can then be used to calculate the average height on the inside the toolpath (h_{in}) and the average height on the outside of the toolpath (h_{out}).

$$h_{in} = h \times d_{in} \tag{5}$$

$$h_{out} = h \times d_{out} \tag{6}$$

The height difference can then be calculated as the difference between h_{in} and h_{out}.

3.5. Curve fitting height data and comparison with geometric expectations

Experimental height difference data for small angles can be accurately fitted assuming an exponential decay with ROI length (see Fig. 4b-d with similar data for larger angles in Supplementary Fig. S3a-b). An exponential decay model can also be used to describe the results from the geometric model described above. Note that the model described above in Section 3.4 uses only relative path lengths for inside and outside volumes and assumes that no self-leveling occurs. As expected from the analysis described in Section 3.2, however, the effects of self-leveling cannot be neglected accurately in this case. This is evident in Fig. 4e-g, where the geometric model over-predicts height differences by over an order of magnitude in some cases. The overprediction is most severe for small angles between the lines and sharp radii, which are of particular interest. As such, this proves that accurate predictions of overfill and underfill in aerosol jet printing requires either physical experiments such as those described here or more sophisticated multi-physics models, where the mechanics of the viscous flow of the printed material in the transient region during drying is considered. As noted before, the aerosol droplets are a few micrometers in diameter and hence expected to undergo high level of evaporation [31]. Evaporation will increase the viscosity of the droplets compared to that of the ink in the vial. The viscosity is difficult, if not impossible to measure during printing. In addition, droplet coalescence occurring during printing is difficult to quantify without specialized high-speed and high-resolution camera that can capture such phenomenon occurring at 1–10 μm length scale and at about 100 m/s. We note that the temperature of printing would affect the drying process and at higher temperatures, we would expect reduced effect of the leveling and vice versa. The wetting of the surface would affect the first layer but is not expected to influence the build-up of the 3D structures. Similarly, the type of substrate is not expected to affect the material accumulation beyond the first layer of the stack. As such, considering the limitations in the in-situ measurements, including the effect of viscosity in a model is beyond the scope of the current work.

3.6. Complex 3D star and Scotty Dog shapes via toolpath strategies

The results from Sections 3.1–3.5 can be used to design toolpath strategies that enable the printing of complex 3D microarchitectures such as a *Star* and a *Scotty Dog*, the Carnegie Mellon University mascot. Sample toolpaths of a given layer of printing for the 3D star and the Scotty Dog are shown in Fig. 5 and 6, respectively. Note that the 3D star design (Fig. 5a-c) covers two different angles of bends in microwalls (one large and one small) and four corner radii; while the 3D Scotty Dog design (Fig. 6a, b) has an irregular shape and covers a range of different corner angles and two corner radii between the microwalls.

For the 3D stars shown in Fig. 5, the printing started with the first layer for the star in Fig. 5a, followed by Fig. 5b, and then Fig. 5c, before returning to printing of the second layer of star in Fig. 5a, and so on. That is in contrast to serial printing in which one structure would be printed in totality before moving to the next structure. In addition, printing of closed contours in Fig. 5 and 6 required that a small gap be introduced between the starting point of the toolpath and its end point for a given layer. This was to avoid aberrations at the locations where the closed contour completes the rotation, i.e., where the shutter opens or closes. Although opening and closing of the shutter and stage motion had minimal effect on the mass accumulation for 2D segments over 100 μm in length (Section 3.1), we found that the gap mentioned above - of the order of ten micrometers - was still necessary to avoid for 3D microwalls that were printed over multiple layers. Implementing shutter-on-the-fly, which is a method to more accurately time the shutter with platen movement by initiating shutter open/close while the stage is still in motion, is a possible alternative to this method, but the manual placement of the shutter between cleanings made this timing less reliable and hence not utilized in this study.

The toolpath in Fig. 5a-c for the 3D Star is inscribed in a 2 mm circle with a printed line width of 20 μm. Each of the outer corners has an angle of 30° between the lines (8 intersections), while each of the inner corners has an angle of 75° (8 intersections). The 3D star shape, thus, has 16 vertical microwall segments with four corner radii on different samples. The top view SEM images of the printed 3D stars at different fillet radii are given in Supplementary Fig. S4a-c.

The AJ printed 3D Stars for different corner radii are shown in Fig. 5d-l. The leftmost panels of Fig. 5 (Fig. 5a, d, g, j) show the material accumulation when no corner radii are applied to the toolpath for either the outer or inner corners. The middle panels of Fig. 5 (Fig. 5b, e, h, k) show the results when a radius of 20 μm (equal to the line width) is applied to the outer corners and a radius of 10 μm (half the line width) is applied to the inner corners. The right set of panels in Fig. 5 (Fig. 5c, f, i, l) show results when a radius of 30 μm is applied to the sharper, outer corners and a radius of 20 μm applied to the inner corners. The corresponding z-height profiles as measured by white-light interferometry are shown in Figs. 5j-5l, with the quantitative measure of the protrusions shown in Fig. 5m. The star printed without a fillet radius shows characteristic protrusions at both the outer and inner corners. There are voids directly adjacent to this overgrowth where the extended material captured aerosol droplets before they could reach the intended deposition location. Further, a small radius on the external side is evident, which is the result of underfill inherent to the line width – this is despite the toolpath itself having no radius in this case. For samples with a small, applied corner radius, we observe no evidence of overgrowth or voids at the corners, and the overall height stays consistent as the printing direction is changed (Fig. 5h, k). The star with the slightly larger radii shows no observable accumulation as well (Fig. 5i, l). This implies that a radius equivalent to the line thickness is sufficient for defect-free printing for this use case which matches well with the predictions from the analyzed 2D data sets in Figs. 3 and 4. The results in Figs. 5j-5m also show that the protrusion for a 36-layer structure, if increase linearly (based on accumulation of a micron per layer in Fig. 4f), would close to 50 μm. In reality, we see an accumulation of about 100 μm accompanied with a void-like structure. Clearly, as the structure is built-up, shadowing effect and lack of substrate constraint would increase the accumulation. More sophisticated models will be required to capture this effect. It is clear, however, that for a corner radius of the order of the thickness eliminates this accumulation as seen in Fig. 5m. To demonstrate the generality of the approach, we also printed stars similar to those shown in Figs. 5a-5c for ZnO ink and Ag ink from another supplier as shown in Supplementary Information, Fig. S5a and S5b, respectively. This result show similar qualitative results – accumulation at the corners eliminated by a corner radius equivalent to about the wall thickness leading to defect-free printing.

A second demonstration consisted of Carnegie Mellon University logo, the Scotty Dog. This design includes 54 microwall segments forming the face, along with 117 crosshatch microwall segments

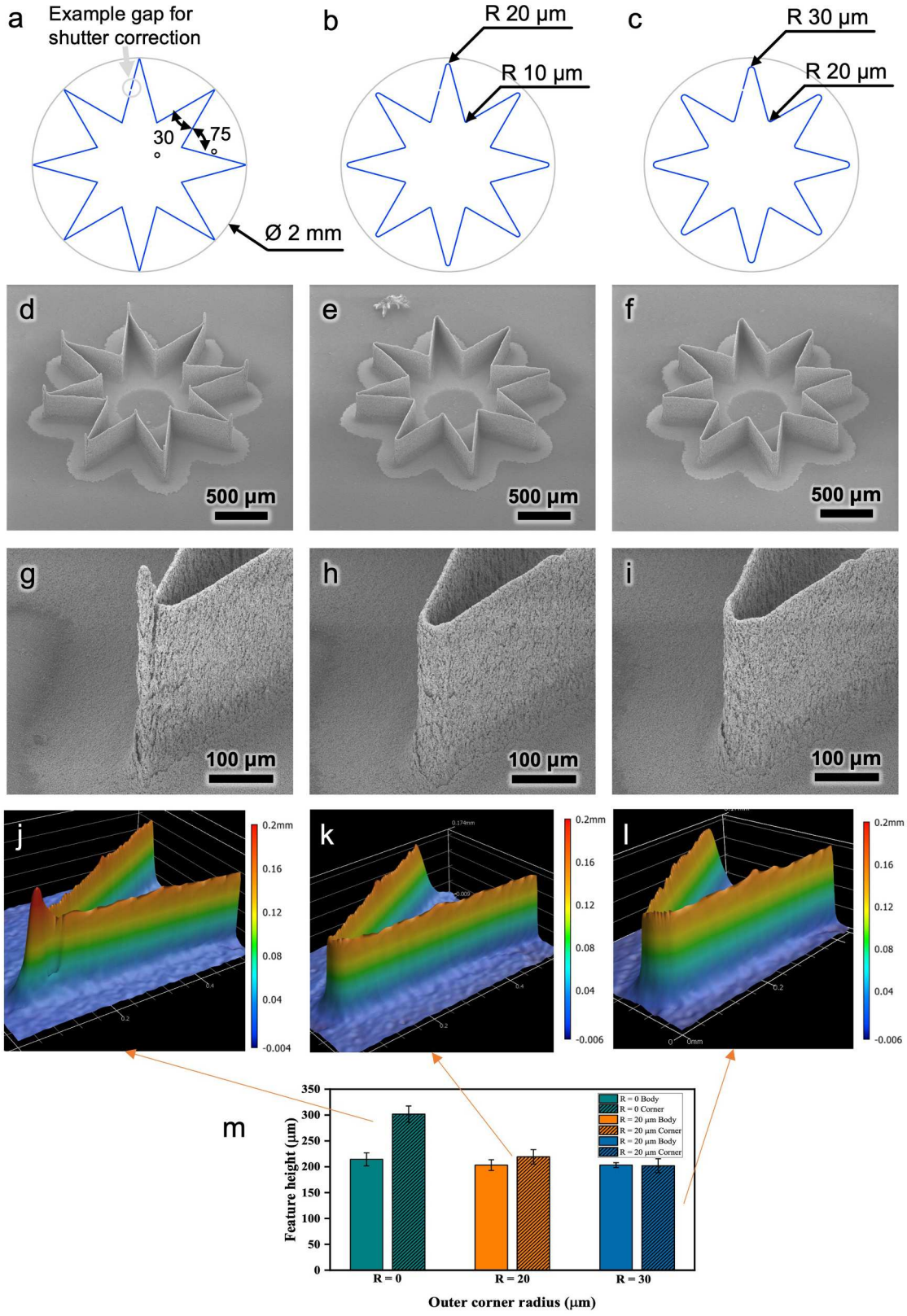

Fig. 5. Realization of high-fidelity 3D architectures based on appropriate AJ printing toolpath strategy. **(a-c)** Schematics of toolpaths used to print a three-dimensional 8-pointed star. Note the gap for shutter opening and closing in the schematics. This gap is moved to different segments (a total of 16 segments) of the star in each case. The printing direction was then reversed after printing of 16 layers to print a total of 32 unique layers. **(d-f)** Perspective SEM of 8-pointed stars with toolpaths shown in Fig. (a-c), respectively. For corresponding top-down SEMs, please see Supplementary Information, Fig. S4a-S4c, respectively. **(g-i)** Close-up images of outer points of the stars shown in (a-c), respectively. **(j-l)** Profile scans of images in (g-h), respectively, as measured white-light interferometry showing presence and absence of material accumulation. **(m)** Quantitative measurement of the height at the corners vs center for R = 0, R = 20 µm and R = 30 µm,

corresponding to images in (j), (k), and (l), respectively. The SEMs of inner corners of the stars in (d-f) are given in Supplementary Information, Fig. S4d-S4f, respectively.

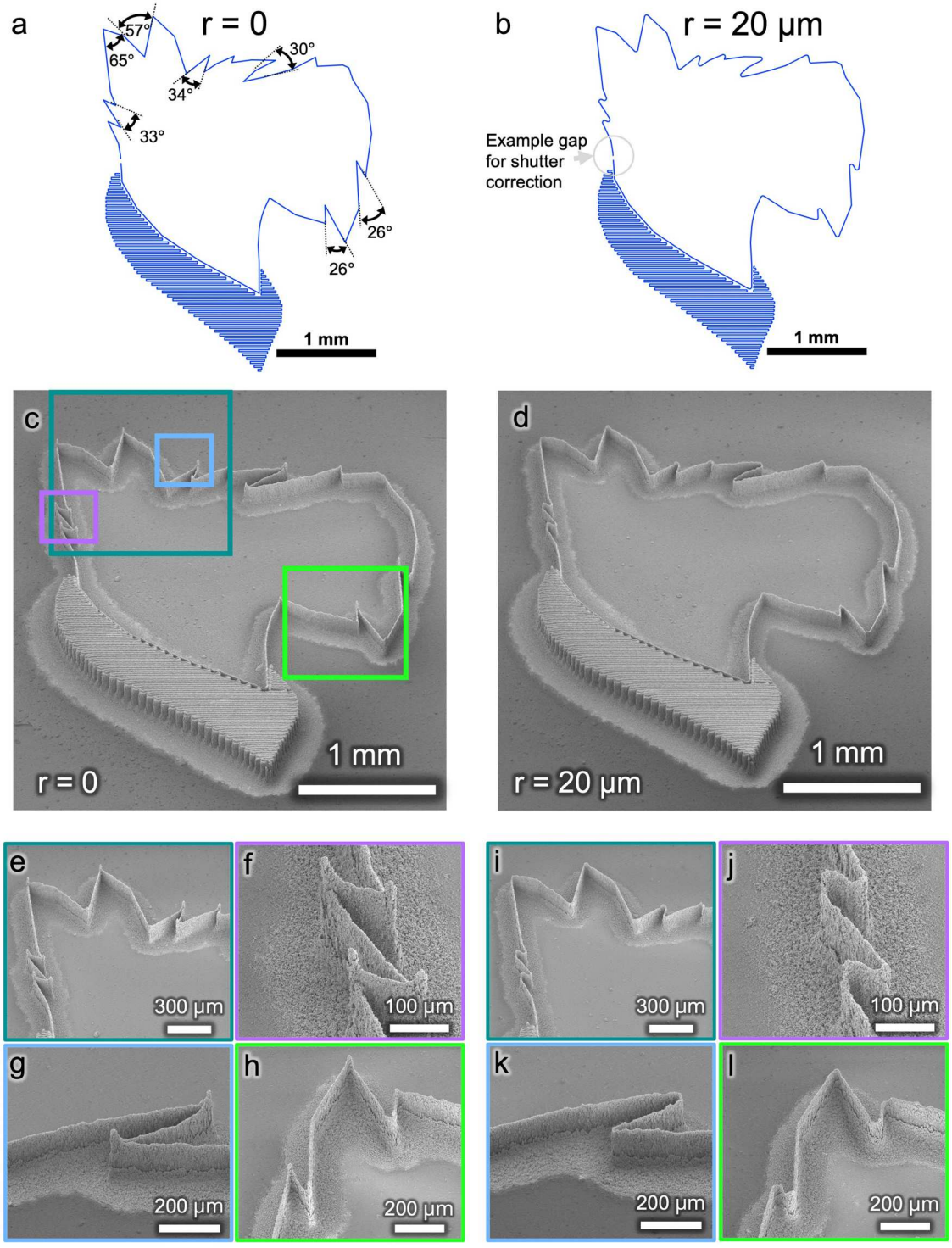

Fig. 6. 3D Scotty Dog, the CMU mascot, AJ printed using different toolpath strategies. (a-b) Schematics of toolpaths for the Scotty Dog, the CMU mascot, for corner radii of 0 µm and 20 µm, respectively. Some example angle values are labeled. Note that the labeled gap for shutter opening and closing is moved to locations without toolpath trajectory changes for each successive layer printed, for a total of 16 locations, for both radii. These 16 layers are printed, and then the direction is reversed for the following 16 layers, using the same gap locations. This creates 32 unique layers in total. (c) Angled view SEM image of CMU's scotty dog logo printed via aerosol jet with a toolpath radius of 0 µm. Walls are all 20 µm thick. (d) Angled view SEM image of CMU's scotty dog logo printed via aerosol jet with a toolpath radius of 20 µm. Walls are all 20 µm thick. (e-h) Close-up images of (c). (i-l) Close-up images of (d).

forming the collar of the dog. These segments (straight and curved) intersected at angles ranging from 26° to 175°. The Scotty Dog design with example toolpaths is shown in Fig. 6a, b. As before, a gap is placed in each layer for the shutter open/close locations and the samples were printed in parallel. In this demonstration, one sample (Fig. 6a, c, and e-h) was printed with no radius applied to the toolpath, and another (Fig. 6b, d, and i-l) was printed with a 20 μm radius applied to all corners. See top views of the printed 3D Scotty Dog images in Supplementary Fig. S6a-c. The printed line width is again 20 μm for this demonstration. From Fig. 6d, it is evident that an application of the fillet radius only minorly alters the overall geometry, even in the region shown in Fig. 6 l with the smallest angle of 26°. As in the previous demonstration (Fig. 5), the sample printed without an added radius showed significant protrusions in all of the tight corners. Adjacent voids/lack of material are particularly evident in Fig. 6 f. The sample with added fillets (Fig. 6j), however, shows a printed geometry with high fidelity to the intended design with no overgrowths or large voids. These demonstrations together show the applicability of the results from 2D line geometries to arbitrary 3D microwall architectures.

The results presented in this work provide important information about toolpath strategies that can be employed to prevent accumulation-related defects when building high-fidelity 3D microarchitectures (e.g., microwalls) via jetting-based AM. The analysis presented in this paper can be suitably modified and utilized for processes such as inkjet printing (where rapid leveling of low viscosity materials could be a significant mechanism), and extrusion printing (e.g., FDM), where nozzle can deform the deposited material and distribute it laterally. Although AJ printing depends on highly complex processes such as ultrasonic atomization, aerosol transport, and droplets that undergo evaporation while being jetted [48], we are able to predict and reproduce defects as desired and mitigate their effects by adding curvature at sharp ends and adding gaps in the toolpath. This is extremely promising in the path towards high-fidelity manufacture of such structures. The data for 2D line segments (Fig. 2) also shows that the information gathered for a single layer of printed material can be used to determine the behavior for 3D structures. We note several approximations in this study. First, we are ignoring effects such as satellite droplet formation, which can affect our prediction, although similar effect on different ink and supplier gives qualitatively similar results regarding material accumulation and its control through toolpath optimization (Supplementary Fig. S5a and S5b). Also, we note that dividing the ROI into sections without angles is a simplification in itself. Although we have observed excellent wetting of silver ink with alumina substrate [33], different calibration may be required for other ink-substrate combinations. Lastly, we also note that the ink leveling/accumulation effect within printed lines will be different for 3D structures (such as walls as in Fig. 5, 6) vs 2D structures (equivalent to 'beads' of lines in Fig. 4) due to substrate constraints. We expect this effect to be prevalent for structure height beyond the thickness (in our case about 20 μm). Our model does not capture it (as it is based purely on material deposition and not leveling, where for beads or for walls). In spite of these approximations, the simple model quantifying the material accumulation described in Section 3.4 qualitatively predicts the presence of protrusion defects due to the difference in the volume of jetted material in different areas of the curved toolpath. This model, however, grossly overestimates the material accumulation. We believe that leveling of the deposited ink droplets on the platen (which is heated to 70°C) prior to the evaporation of the solvents is responsible for the reduction in accumulation of the defects. Printing at lower temperatures will prevent the formation of 3D structures (as drying of the ink in one layer is necessary prior to the deposition of the next layer). Printing at higher temperatures, however, is also expected to accelerate drying of the specific ink [53] possibly leading to less self-leveling, and worsening of the accumulation defects. There is thus a fine balance between the rheology of the deposited ink droplets, heat from the platen, and surface forces that allows formation of the beautiful 3D structures shown in Fig. 5 and 6. Further research is thus needed to fully understand the dynamics of 3D structure formation and the effect of self-leveling for specific inks during AJ printing, which will be part of a future investigation.

The results presented in this paper provide a path for repeatable and defect-free microfabrication of 3D architectures and devices via AJ printing. AJ printed 3D devices have already led to advances in a diverse set of applications such as low-loss passives (i.e., antennas and capacitors) directly printed on Si-chips [39], advanced 3D microelectronic packages [54], first Bain-Computer Interface (BCI) device that can capture electrical signals from throughout the 3D volume of the brain [33], world's fastest biomolecule sensor [35], and ultrathick electrode Li-ion batteries [55]. In general, the expansion of the design space and manufacturing capabilities enabled by this research will open new applications and create advanced solutions for a wide range of engineering problems.

4. Conclusions

In this work, we quantify the effects of toolpath strategies on the formation of large-scale defects for bent structures in AJ printed 3D microarchitectures. The key conclusions of the paper are:

- Build defects for AJ printed 3D microarchitectures with curved segments can be anticipated based on the physics of the printing process. Toolpath strategies can then be implemented to minimize or avoid such defects and realize high-fidelity fabrication of 3D microarchitectures.
- A minimum fillet radius is required to avoid accumulation and void defects for sharp, curved microwall segments of the toolpath. In the present work, these values are identified as,
  - o For 3D microwalls at a 30° angle and forming a bend, a fillet radius equal to the line thickness (or larger) should be applied to avoid build defects during 3D printing.
  - o For 3D microwalls at a 45° angle and forming a bend, a fillet radius equal to half of the line thickness (or larger) should be applied to avoid build defects during 3D printing.
  - o For 3D microwalls at a 90° angle or larger and forming a bend, overfill and underfill effects are negligible, and no fillet radii is required during 3D printing.
  - o For 3D microwalls at a sharper, 15° angle, and forming a bend, adding a small fillet radius is an insufficient solution. These lines should be approximated as single individual lines.
- The effects of stage acceleration and deceleration during the printing of the curved segments are negligible on build defects for the specific parameters (e.g., platen speed of 1 mm/s and ROI $>$ 100 μm) used in this study.
- The mechanics of defect formation in the buildup of curved 3D microarchitectures is rather complex and cannot be fully captured by a simple model that considers the volume of the jetted material. Such a model correctly predicts the presence of defects although it tends to overpredict the defect dimensions significantly. We speculate that ink self-leveling, which is ignored in such a model, plays an important role in reducing the defects in the printed structure; an advantage in ink-based printing.
- AJ printing of the 3D star shape for Ag ink from two suppliers and ZnO ink and the Scotty Dog shape demonstrated in this work highlight the expansion of the design space and microfabrication capabilities for 3D structures via jetting-based AM techniques. In turn, these results will positively contribute to the fields of microelectronic and biomedical devices, electronics packaging, energy storage devices, and surface-sensitive electrochemical systems.

Author contributions

R.P. directed the research. S.R. carried out all the work including

experimental design, printing program development and execution, data analysis, and model development. S.R. wrote the first draft of the paper. C.H. carried out the printing of silver inks from additional supplier and ceramic ink and obtained their protrusion profiles. All authors interpreted the results and edited the manuscript.

Funding

This research was partially funded by Air Force Office of Scientific Research (AFOSR) and Clarkson Aerospace under grant AWD00001291, award #FA9550-21-1-0460, NIH R01 grant #RF1NS110483, and NSF CMMI grant #2328678.

CRediT authorship contribution statement

Sandra M. Ritchie: Writing – review & editing, Writing – original draft, Visualization, Methodology, Investigation, Formal analysis, Data curation. **Chunshan Hu:** Formal analysis, Validation, Writing – review & editing. **Rahul Panat:** Writing – review & editing, Supervision, Project administration, Funding acquisition, Conceptualization.

Declaration of Competing Interest

The authors declare that they have no known competing financial interests or personal relationships that could have appeared to influence the work reported in this paper.

Acknowledgements

We acknowledge partial funding from NIH R01 grant #RF1NS110483, U.S. Air Force Office of Scientific Research (AFOSR) and Clarkson Aerospace under award #FA9550–21–1–0460, and NSF CMMI grant #2328678.

Appendix A. Supporting information

Supplementary data associated with this article can be found in the online version at doi:10.1016/j.addma.2024.104549.

Data Availability

Data will be made available on request.

References

[1] S.S. Alghamdi, S. John, N.R. Choudhury, N.K. Dutta, Additive manufacturing of polymer materials: progress, promise and challenges, Polymers 13 (5) (2021) 39.
[2] A. García-Collado, J.M. Blanco, M.K. Gupta, R. Dorado-Vicente, Advances in polymers based multi-material additive-manufacturing techniques: state-of-art review on properties and applications, Addit. Manuf. 50 (2022) 14.
[3] P. Moghimian, T. Poirie, J. Kroeger, F. Marion, F. Larouche, Emerging functional metals in additive manufacturing, Adv. Eng. Mater. 25 (11) (2023) 14.
[4] T. Özel, H. Shokri, R. Loizeau, A review on wire-fed directed energy deposition based metal additive manufacturing, J. Manuf. Mater. Process. 7 (1) (2023) 24.
[5] H. Ramazani, A. Kami, Metal, FDM, a new extrusion-based additive manufacturing technology for manufacturing of metallic parts: a review, Prog. Addit. Manuf. 7 (4) (2022) 609–626.
[6] J.A. Gonzalez, J. Mireles, Y. Lin, R.B. Wicker, Characterization of ceramic components fabricated using binder jetting additive manufacturing technology, Ceram. Int. 42 (9) (2016) 10559–10564.
[7] R.P. Chaudhary, C. Parameswaran, M. Idrees, A.S. Rasaki, C.Y. Liu, Z.W. Chen, P. Colombo, Additive manufacturing of polymer-derived ceramics: materials, technologies, properties and potential applications, Prog. Mater. Sci. 128 (2022) 54.
[8] T. Mukherjee, J.W. Elmer, H. Wei, T.J. Lienert, W. Zhang, S. Kou, T. DebRoy, Control of grain structure, phases, and defects in additive manufacturing of high-performance metallic components, Prog. Mater. Sci. 138 (2023) 107.
[9] B. He, C. Bi, X.D. Li, W. Wang, G. Yang, , Residual stresses and deformations of laser additive manufactured metal parts: a review, Int. J. Mater. Form. 16 (1) (2023) 14.
[10] H. Yeung, F.H. Kim, M.A. Donmez, J. Neira, Keyhole pores reduction in laser powder bed fusion additive manufacturing of nickel alloy 625, Int. J. Mach. Tools Manuf. 183 (2022) 13.
[11] W.B. Han, M.A. Jafari, S.C. Danforth, A. Safari, Tool path-based deposition planning in fused deposition processes, J. Manuf. Sci. Eng. -Trans. ASME 124 (2) (2002) 462–472.
[12] X.C. Sun, M. Mazur, C.T. Cheng, A review of void reduction strategies in material extrusion-based additive manufacturing, Addit. Manuf. 67 (2023) 14.
[13] Y. Jin, J. Du, Z. Ma, A. Liu, Y. He, An optimization approach for path planning of high-quality and uniform additive manufacturing, Int. J. Adv. Manuf. Technol. 92 (1-4) (2017) 651–662.
[14] Y.A. Wang, C.X. Hu, Z. Wang, S.Z. Lin, Z.Y. Zhao, W.X. Zhao, K.H. Hu, Z.Y. Huang, Y. Zhu, Z.G. Lu, Optimization-based non-equidistant toolpath planning for robotic additive manufacturing with non-underfill orientation, Robot. Comput. -Integr. Manuf. 84 (2023).
[15] Y. Xiong, S.I. Park, S. Padmanathan, A.G. Dharmawan, S. Foong, D.W. Rosen, G. S. Soh, Process planning for adaptive contour parallel toolpath in additive manufacturing with variable bead width, Int. J. Adv. Manuf. Technol. 105 (10) (2019) 4159–4170.
[16] Y.-a Jin, Y. He, J.-z Fu, W.-f Gan, Z.-w Lin, Optimization of tool-path generation for material extrusion-based additive manufacturing technology, Addit. Manuf. 1 (2014) 32–47.
[17] S. Garzon-Hernandez, D. Garcia-Gonzalez, A. Jérusalem, A. Arias, Design of FDM 3D printed polymers: An experimental-modelling methodology for the prediction of mechanical properties, Mater. Des. 188 (2020) 10.
[18] K. Elhattab, S.B. Bhaduri, P. Sikder, Influence of fused deposition modelling nozzle temperature on the rheology and mechanical properties of 3D printed β-tricalcium phosphate (TCP)/polylactic acid (PLA) composite, Polymers 14 (6) (2022) 18.
[19] M.T. Rahman, C.Y. Chen, B. Karagoz, M. Renn, M. Schrandt, A. Gellman, R. Panat, High performance flexible temperature sensors via nanoparticle printing, Acs Appl. Nano Mater. 2 (5) (2019) 3280–3291.
[20] K. Parate, S.V. Rangnekar, D.P. Jing, D.L. Mendivelso-Perez, S.W. Ding, E.B. Secor, E.A. Smith, J.M. Hostetter, M.C. Hersam, J.C. Claussen, Aerosol-jet-printed graphene immunosensor for label-free cytokine monitoring in serum, Acs Appl. Mater. Interfaces 12 (7) (2020) 8592–8603.
[21] L. Gamba, J.A. Lajoie, T.R. Sippel, E.B. Secor, Multi-material aerosol jet printing of Al/cuo nanothermites for versatile fabrication of energetic antennas, Adv. Funct. Mater. 8 (2023).
[22] E.B. Secor, N.S. Bell, M.P. Romero, R.R. Tafoya, T.H. Nguyen, T.J. Boyle, Titanium hydride nanoparticles and nanoinks for aerosol jet printed electronics, Nanoscale 14 (35) (2022) 12651–12657.
[23] N. Turan, M. Saeidi-Javash, J.H. Chen, M.X. Zeng, Y.L. Zhang, D.B. Go, Atmospheric pressure and ambient temperature plasma jet sintering of aerosol jet printed silver nanoparticles, Acs Appl. Mater. Interfaces 13 (39) (2021) 47244–47251.
[24] N. Kempf, Y.L. Zhang, Aerosol jet printed 3 omega sensors for thermal conductivity measurement, Rev. Sci. Instrum. 92 (10) (2021) 7.
[25] M. Saeidi-Javash, Y.P. Du, M.X. Zeng, B.C. Wyatt, B.W. Zhang, N. Kempf, B. Anasori, Y.L. Zhang, All-printed MXene-graphene nanosheet-based bimodal sensors for simultaneous strain and temperature sensing, ACS Appl. Electron. Mater. 3 (5) (2021) 2341–2348.
[26] J.H. Chen, M. Saeidi-Javash, M. Palei, M.X. Zeng, Y.P. Du, K. Mondal, M. D. McMurtrey, A.J. Hoffman, Y.L. Zhang, Printing noble metal alloy films with compositional gradient, Appl. Mater. Today 27 (2022) 7.
[27] S. Khan, T.P. Nguyen, M. Lubej, L. Thiery, P. Vairac, D. Briand, Low-power printed micro-hotplates through aerosol jetting of gold on thin polyimide membranes, Microelectron. Eng. 194 (2018) 71–78.
[28] Y.C. Zhu, L.K. Yu, D.Z. Wu, W.L. Lv, L.Y. Wang, A high-sensitivity graphene ammonia sensor via aerosol jet printing, Sens. Actuator A-Phys. 318 (2021) 10.
[29] E. Jabari, E. Toyserkani, Aerosol-Jet printing of highly flexible and conductive graphene/silver patterns, Mater. Lett. 174 (2016) 40–43.
[30] R. Eckstein, G. Hernandez-Sosa, U. Lemmer, N. Mechau, Aerosol jet printed top grids for organic optoelectronic devices, Org. Electron. 15 (9) (2014) 2135–2140.
[31] M.S. Saleh, C.S. Hu, R. Panat, Three-dimensional microarchitected materials and devices using nanoparticle assembly by pointwise spatial printing, Sci. Adv. 3 (3) (2017) 8.
[32] M.S. Saleh, M. HamidVishkasougheh, H. Zbib, R. Panat, Polycrystalline micropillars by a novel 3-D printing method and their behavior under compressive loads, Scr. Mater. 149 (2018) 144–149.
[33] M.S. Saleh, S.M. Ritchie, M.A. Nicholas, H.L. Gordon, C. Hu, S. Jahan, B. Yuan, R. Bezbaruah, J.W. Reddy, Z. Ahmed, M. Chamanzar, E.A. Yttri, R.P. Panat, CMU Array: A 3D nanoprinted, fully customizable high-density microelectrode array platform, Sci. Adv. 8 (40) (2022) eabj4853.
[34] S.M. Ritchie, S. Kovacevic, P. Deshmukh, A.D. Christodoulides, J.A. Malen, S. D. Mesarovic, R.P. Panat, Shape distortion in sintering results from nonhomogeneous temperature activating a long-range mass transport, Nat. Commun. 14 (1) (2023).
[35] M.A. Ali, C.S. Hu, S. Jahan, B. Yuan, M.S. Saleh, E.G. Ju, S.J. Gao, R. Panat, Sensing of COVID-19 antibodies in seconds via aerosol jet nanoprinted reduced-graphene-oxide-coated 3D electrodes, Adv. Mater. 33 (7) (2021) 15.
[36] M.A. Ali, C.S. Hu, B. Yuan, S. Jahan, M.S. Saleh, Z.T. Guo, A.J. Gellman, R. Panat, Breaking the barrier to biomolecule limit-of-detection via 3D printed multi-length-scale graphene-coated electrodes, Nat. Commun. 12 (1) (2021) 16.
[37] M.S. Saleh, J. Li, J. Park, R. Panat, 3D printed hierarchically-porous microlattice electrode materials for exceptionally high specific capacity and areal capacity lithium ion batteries, Addit. Manuf. 23 (2018) 70–78.

[38] M.S. Saleh, C.S. Hu, J. Brenneman, A. Al Mutairi, R. Panat, 3D printed three-dimensional metallic microlattices with controlled and tunable mechanical properties, Addit. Manuf. 39 (2021) 16.
[39] T. Rahman, L. Renaud, D. Heo, M. Renn, R. Panat, Aerosol based direct-write micro-additive fabrication method for sub-mm 3D metal-dielectric structures, J. Micromech. Microeng. 25 (10) (2015) 8.
[40] Y. Gu, D.R. Hines, V. Yun, M. Antoniak, S. Das, Aerosol-jet printed fillets for well-formed electrical connections between different leveled surfaces, Adv. Mater. Technol. 2 (11) (2017) 1700178.
[41] R.R. Tafoya, E.B. Secor, Understanding and mitigating process drift in aerosol jet printing, Flex. Print. Electron. 5 (1) (2020) 015009.
[42] E.B. Secor, Light scattering measurements to support real-time monitoring and closed-loop control of aerosol jet printing, Addit. Manuf. 44 (2021) 7.
[43] J.D. Rurup, E.B. Secor, Predicting deposition rate and closing the loop on aerosol jet printing with in-line light scattering measurements, Adv. Eng. Mater. 25 (12) (2023) 10.
[44] B.A. Lariviere, P.W. Groth, P.C. Joshi, M.N. Ericson, An optical aerosol sensor for process monitoring of aerosol-jet printing, IEEE Access 11 (2023) 99159–99167.
[45] M.S. Saleh, S.M. Ritchie, M.A. Nicholas, H.L. Gordon, C. Hu, S. Jahan, B. Yuan, R. Bezbaruah, J.W. Reddy, Z. Ahmed, CMU Array: A 3D nanoprinted, fully customizable high-density microelectrode array platform, Sci. Adv. 8 (40) (2022) eabj4853.
[46] M.A. Ali, C. Hu, B. Yuan, S. Jahan, M.S. Saleh, Z. Guo, A.J. Gellman, R. Panat, Breaking the barrier to biomolecule limit-of-detection via 3D printed multi-length-scale graphene-coated electrodes, Nat. Commun. 12 (1) (2021) 7077.
[47] J. Brenneman, D.Z. Tansel, G.K. Fedder, R. Panat, High-conductivity crack-free 3D electrical interconnects directly printed on soft PDMS substrates, Adv. Mater. Technol. 7 (12) (2022) 2200396.
[48] E.B. Secor, Principles of aerosol jet printing, Flex. Print. Electron. 3 (3) (2018) 12.
[49] J.Q. Feng, Mist flow visualization for round jets in Aerosol Jet® printing, Aerosol Sci. Technol. 53 (1) (2019) 45–52.
[50] R. Comminal, M.P. Serdeczny, D.B. Pedersen, J. Spangenberg, Motion planning and numerical simulation of material deposition at corners in extrusion additive manufacturing, Addit. Manuf. 29 (2019) 17.
[51] D. Montoya-Zapata, J. Posada, P. Alvarez, C. Creus, A. Moreno, I. Ortiz, O. Ruiz-Salguero, Experimental and computational assessment of minimizing overfill in trajectory corners by laser velocity control of laser cladding, Int. J. Adv. Manuf. Technol. 119 (9-10) (2022) 6393–6411.
[52] J.M. Hoey, A. Lutfurakhmanov, D.L. Schulz, I.S. Akhatov, A review on aerosol-based direct-write and its applications for microelectronics, J. Nanotechnol. 2012 (1) (2012) 324380.
[53] M.S. Saleh, C. Hu, R. Panat, Three-dimensional microarchitected materials and devices using nanoparticle assembly by pointwise spatial printing, Sci. Adv. 3 (3) (2017) e1601986, https://doi.org/10.1126/sciadv.1601986).
[54] A. Glushkova, P. Andričević, R. Smajda, B. Náfrádi, M. Kollár, V. Djokić, A. Arakcheeva, L. Forró, R. Pugin, E. Horváth, Ultrasensitive 3D aerosol-jet-printed perovskite X-ray photodetector, ACS Nano 15 (3) (2021) 4077–4084.
[55] T.S. Wei, B.Y. Ahn, J. Grotto, J.A. Lewis, 3D printing of customized Li-ion batteries with thick electrodes, Adv. Mater. 30 (16) (2018) 7.